An Imaging Method for Spaceborne Cooperative Multistatic SAR Formations With Nonzero Cross-Track Baselines

Haoyu Lin, Yunkai Deng, *Member, IEEE*, Heng Zhang, *Member, IEEE*, Da Liang, *Member, IEEE*, and Xiaoxue Jia

***Abstract*—Spaceborne multistatic synthetic aperture radar (M-SAR) formations can deploy multiple spatially separated receiving phase centers along the along-track (AT) direction to achieve high-resolution wide-swath. However, the cross-track (XT) separation between the spacecraft is inevitable due to the formation design like orbital safety and application potential like the XT interferometry. In addition, the different motion vectors of two or more satellites caused by the Helix formation will lead to the difference of the Doppler parameters at the same range gate. Therefore, nonzero XT baselines and space-variant characteristics pose new challenges to the focusing and phase-preserving of the M-SAR imaging. To this end, an imaging method for spaceborne cooperative M-SAR formations with nonzero XT baselines is proposed in this article. Firstly, a spaceborne cooperative M-SAR formation is demonstrated. Afterward, the imaging method is described in detail. The motion compensation technology and the idea of partitioned equivalent velocity are adopted to solve the problems of nonzero XT baselines and space-variant characteristics, respectively. Finally, the simulations of point targets and distributed targets are carried out to verify the proposed method, and the results show that the precise focusing of spaceborne cooperative M-SAR with nonzero XT baselines can be achieved by the proposed imaging method.**

***Index Terms*—M-SAR formations, M-SAR imaging processing, multistatic synthetic aperture radar (M-SAR), nonzero cross-track (XT) baselines.**

I. Introduction

SPACEBORNE multistatic synthetic aperture radar (SAR) is an extension of the concept of bistatic SAR (BiSAR), which is characterized by deploying multiple physically separate transceiver to obtain three or more simultaneous echo datasets [1], [2]. Multistatic SAR (M-SAR) has many unique characteristics that meet the application requirements of the next-generation spaceborne SAR system, such as high-resolution wide-swath (HRWS) imaging, along-track (AT) interferometry, cross-track (XT) interferometry, and so on, so it has received extensive attention [3], [4], [5]. Another trend is adopting cheaper systems with the intention to shift the complexity from the space segment to software. Thus, small satellites which received echoes only can be deployed in the formation of M-SAR systems to provide equivalent or superior performance compared to the state-of-the-art SAR systems currently with a minor cost and higher robustness toward failure [6].

The processing methods of spaceborne M-SAR data have been studied by several scholars, and the main purpose is to use the M-SAR data to overcome the contradiction between the swath width and the azimuth resolution of the conventional SAR systems. The reconstruction method proposed in [7] can be used in the case of AT displaced receivers, and Sakar et al. proposed a reconstruction method for M-SAR formation with large AT baselines [8], [9]. In [10], a reconstruction scheme in the 2-D frequency domain is introduced, which is also aimed to the case of AT baselines. However, the XT separation between the spacecraft may be intentional when the spacecrafts are operating in cooperative formations, so that along-track drifts can be tolerated without increasing the collision risk. More importantly, it can form a single-pass XT interferometry system, which has broad application prospects. Unfortunately, a large difference of the slant range history between secondary satellites is produced due to XT baselines, so the existence of XT baselines will bring difficulties to the subsequent imaging processing. The most troublesome problem is that the additional azimuth modulation phase introduced by XT baselines will make the existing reconstruction methods used only for AT direction failure. Some scholars have put forward some ideas to solve this problem. Dogan et al. [11] provided a processing method in the case of nonzero XT baselines, but the derivation of the method is carried out under the assumption of flat earth. In [12], the errors introduced by XT baselines were modeled as channel mismatches, and a compensation method is proposed. However, the model established in [12] is based on the traditional monostatic multichannel system, i.e., receiving apertures are distributed in one platform, so the method proposed in [12] is only practicable for the case where XT baselines are very

Manuscript received 26 July 2022; revised 13 September 2022; accepted 30 September 2022. Date of publication 4 October 2022; date of current version 12 October 2022. This work was supported in part by the National Natural Science Fund under Grant 61901443. *(Corresponding author: Heng Zhang.)*

Haoyu Lin, Yunkai Deng, Heng Zhang, and Xiaoxue Jia are with the Department of Space Microwave Remote Sensing System, Aerospace Information Research Institute, Chinese Academy of Sciences, Beijing 100190, China, and also with the School of Electronic, Electrical and Communication Engineering, University of Chinese Academy of Sciences, Beijing 100039, China (e-mail: lhyjack@163.com; ykdeng@mail.ie.ac.cn; zhangheng@aircas.ac.cn; xiaoxue_snowing@163.com).

Da Liang is with the College of Marine Technology, Faculty of Information Science and Engineering, Ocean University of China, Qingdao 266100, China (e-mail: daliang16@foxmail.com).

Digital Object Identifier 10.1109/JSTARS.2022.3211854

small (less than 10 m). There are other efforts for the problem of nonzero XT baselines, which is mentioned in [10], [13], [14], but no complete solution is given.

For the imaging algorithm, since the cooperative M-SAR system also satisfies the quasi-stationary configuration, so many existing BiSAR imaging algorithms can be considered, such as Loffeld's bistatic formula (LBF) method [15], [16], extended LBF method [17], [18], series reversion [19], [20], and so on. However, there are still some problems. The different motion vectors of two or more satellites caused by the Helix satellite formation will lead to the difference of the closest slant range and Doppler characteristics at the same range gate. In more general terms, the azimuth modulations are unequal for the primary and secondary satellites due to the different slant ranges and velocities, which is described as the problem of space-variant characteristics in this article. However, the imaging algorithms mentioned above cannot solve the problem of space-variant characteristics well.

In this article, an imaging method for spaceborne cooperative M-SAR formations with nonzero XT baselines is proposed under the assumption that the error of elevation accuracy is zero, and the unambiguous recovery of the M-SAR data and the problem of space-variant characteristics are aimed to be solved. Firstly, remove the extra phase error in the echo data caused by nonzero XT baselines. Since nonzero XT baselines are similar to the motion error, so it is possible to consider applying Motion Compensation (MoCo) technology to compensate for the extra phase error introduced by XT baselines [21], [22]. After that, the case of nonzero XT baselines is converted to the case of zero XT baselines, and many mature reconstruction methods for the data of AT displacements can be used to obtain the unambiguous echo signal. Secondly, an imaging algorithm based on the idea of *partitioned equivalent velocity* instead of the hyperbolic range history framework is proposed, which refers to the quasi-monostatic method proposed by Bamler et al. [23], and the range-variant and azimuth-variant *equivalent velocity* is used to solve the problem of space-variant characteristics in the Bi/M-SAR imaging.

This article is arranged as follows. In Section II, a kind of spaceborne cooperative M-SAR formations with nonzero XT baselines is demonstrated, and the problem brought by nonzero XT baselines is discussed. An imaging method for spaceborne cooperative M-SAR formations with nonzero XT baselines is proposed in Section III. The simulations of point targets and distributed targets are carried out in Section IV to verify the proposed method. Finally, Section V concludes the article.

II. Formation and Problem

Although spaceborne cooperative M-SAR formation with nonzero XT baselines can provide many application potentials that cannot be ignored, it brings some difficulties of signal processing. Therefore, a kind of spaceborne cooperative M-SAR formation is demonstrated firstly, and the coverage capability of this formation is given. Then, the problem caused by nonzero XT baselines is also discussed.

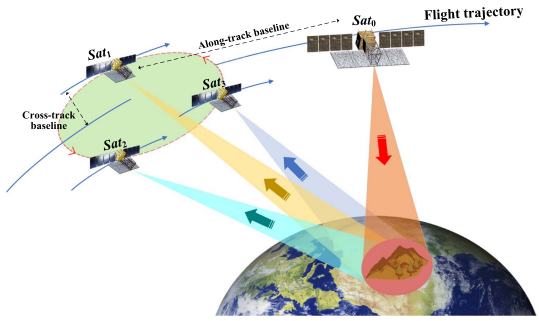

Fig. 1. Artist's view of the multibaselines interferometry of an cooperative M-SAR formation. "Sat_0" refers to the primary satellite, and "Sat_n" ($n = 1, 2, 3$) refers to the secondary satellite. n denotes the nth secondary satellite.

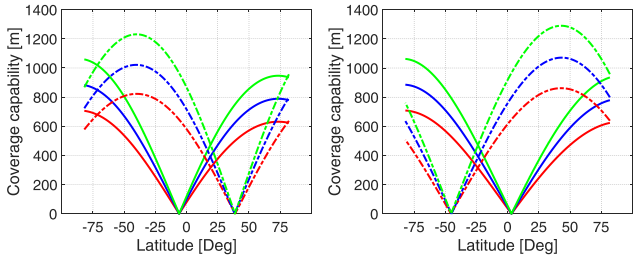

Fig. 2. Coverage capability of the proposed M-SAR formation for low latitudes under the case of (a) ascending orbit and (b) descending orbit. Three colors represent three sets of configurations, i.e., the red, blue, and green lines refer to configurations of Sat_0-Sat_1, Sat_0-Sat_2, and Sat_0-Sat_3, respectively. The solid and dashed lines represent the XT and AT baselines, respectively.

A. Formation Configuration

A conceptual diagram of an M-SAR formation applied to multibaselines interferometry is given in Fig. 1. The formation consists of a primary satellite, which transmits radar signals and three secondary satellites which receive echo signals only. In the proposed M-SAR formation, the three secondary satellites follow the primary satellite in a cooperative formation, and the flexible baselines can be selected between them. In addition, the inherent system limitation of HRWS imaging is overcome by placing the receiving phase centers on separate small satellites. For the convenience of expression, Sat_0 is used to represent the primary satellite, and Sat_n ($n = 1, 2, 3$) is used to denote the nth secondary satellite.

The Helix formation can be adopted in the proposed formation, which uses the double-Helix formation of TanDEM-X for [24]. The coverage capability of the proposed formation is analyzed in Fig. 2. The specific configurations of the low-latitude formation are taken as an example, and the six orbital elements of the proposed M-SAR formation are shown in Table I. Three sets of configurations are formed by the coordination of baselines between the Sat_0 and Sat_n, and they are represented by the lines of three colors in Fig. 2.

B. Problem

Usually, the control in XT baselines has to take into account the topographic variations within the footprint, since topography

TABLE I
SIX ORBITAL ELEMENTS OF THE PROPOSED M-SAR FORMATION. a, e, I, ω, AND Ω REPRESENT THE SEMIMAJOR AXIS, ECCENTRICITY, ARGUMENT OF PERIGEE, RIGHT ASCENSION OF ASCENDING NODE, AND MEAN ANOMALY, RESPECTIVELY

Parameters	Sat_0	Sat_1	Sat_2	Sat_3
a (km)	7354.4884	7354.4884	7354.4884	7354.4884
e	0.001087	0.001051	0.001043	0.001034
I (°)	99.3938	99.3938	99.3938	99.3938
ω (°)	10.0000	12.385133	13.006672	13.638538
Ω (°)	11.0921	11.097391	11.098713	11.100036
M (°)	90.0000	87.615731	86.994408	86.362758

"Sat_0" refers to the primary satellite, and Sat_n denotes the nth secondary satellite, $n \in 1, 2, 3$.

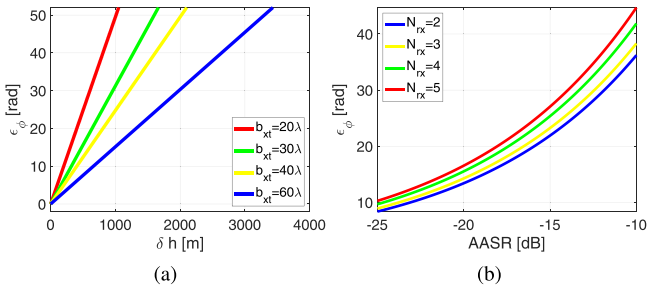

Fig. 3. Impacts of the XT baseline b_{xt} in terms of the phase error [25]. (a) The phase error ε_ϕ changes with the topographic variation δh and the XT baseline b_{xt}. (b) The phase error ε_ϕ changes with and the AASR and the number of satellites N_{rx}.

imposes an inherent model mismatch in the reconstruction process. Thus, the XT baseline must be strictly controlled to obtain the high-quality M-SAR image, which was analyzed in detail in [25]. The requirement on the orbital tube for the constellation can be approximated as follows [25]:

$$b_{xt} \approx \frac{\varepsilon_\phi\left(\mathrm{AASR}, N_{rx}\right)}{\pi} \cdot \frac{\lambda \cdot R_0 \cdot \sin\theta_i}{\delta h} \tag{1}$$

where $\varepsilon_\phi(\mathrm{AASR}, N_{rx})$[1] is the maximum phase excursion, which can be tolerated within the elements of the constellation, and the value of ε_ϕ is a design parameter, which depends on the Azimuth-Ambiguity-to-Signal Ratio (AASR) value of the system specification and the number of satellites N_{rx} in the formation; R_0 is the near slant range; θ_i is the near incidence; δh refers to the maximum topographic variation within the scene.

When the error introduced by the XT baseline is not compensated, the XT baseline b_{xt} is needed to be strictly limited due to the topographic variation δh, the AASR, and the number of satellites N_{rx}. The impact of the XT baseline as a function of the phase error is shown in Fig. 3. Fig. 3(a) shows the phase error ε_ϕ changes with the topographic variation δh and the XT baseline b_{xt}, and it is calculated assuming a formation of two satellites. The relation between the phase error and the AASR for different constellation sizes is illustrated in Fig. 3(b).

More detailed analysis on the orbit control sensitivity of SAR systems in different frequency bands is given in [25], and the conclusion is that a threshold between 10λ and 20λ covering topographic variations up to 1–2 km is an acceptable compromise when the compensation of nonzero XT baselines is not considered, where λ is carrier wavelength. Otherwise, the azimuth ambiguity level of the reconstructed signal will raise dramatically. However, the applications potential of too short XT baselines (5 m in L-band and 0.6 m in X-band) is limited in the M-SAR system used for the multibaselines interferometry. Thus, the problem to be considered is how to compensate for the extra phase error introduced by XT baselines when they are further increased. For the proposed formation in this article, phase errors caused by the difference of the slant range history due to nonzero XT baselines are shown in Fig. 4. Obviously, larger XT baselines will produce nonnegligible phase errors, which causes the reconstruction process to fail. Therefore, the method proposed in this article can eliminate these phase errors to achieve fine focusing of spaceborne cooperative M-SAR formations with nonzero XT baselines.

[1]The equation results from the height to phase conversion of a half-baseline interferometer, which can refer to [26].

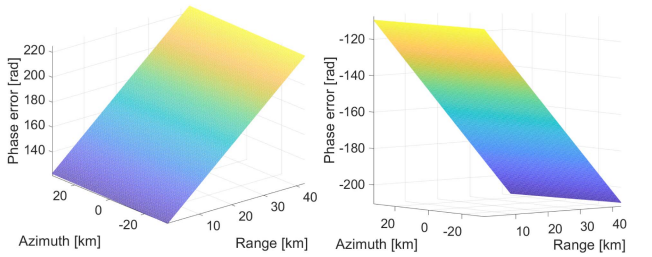

Fig. 4. Phase error caused by the difference of the slant range history due to nonzero XT baselines, and XT baselines are about 20 m for the L-band M-SAR system. (a) The case of the secondary satellite Sat_1. (b) The case of the secondary satellite Sat_2.

III. DATA PROCESSING

In this section, an imaging method for spaceborne cooperative M-SAR formations with nonzero XT baselines is proposed, and the diagram of the data processing is shown in Fig. 5.

A. Preprocessing

Two tasks, i.e., synchronization phase error compensation and platform mismatch calibration, are needed to be completed in the preprocessing step.

1) Synchronization Phase Error Compensation: The independent oscillators are used in the transmitter and receivers, and any deviation between the oscillators will cause a residual modulation of the recorded SAR raw data [27], [28]. An advanced noninterrupted synchronization scheme is adopted in the LuTan-1 (LT-1) mission [29], and the LT-1 is a spaceborne BiSAR mission. For the spaceborne cooperative M-SAR system, the synchronization scheme used in the current BiSAR system can be used for reference. Pulse compression is firstly performed to the synchronization signals and the peak phases are extracted in the compressed synchronization signals. Then, orbit parameters are used to correct the Doppler effects and the relativistic effect [30]. Afterward, the coarse-compensation phase can be

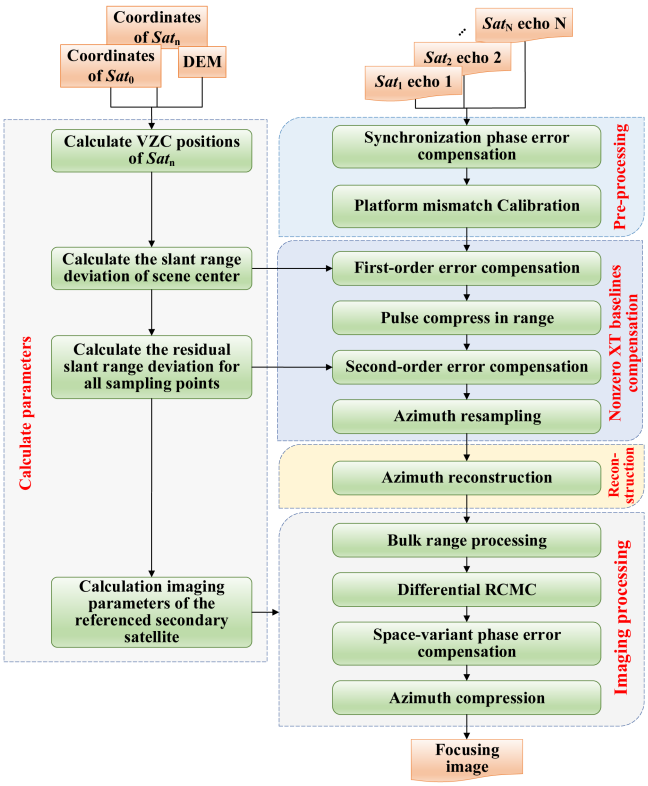

Fig. 5. Diagram of the data processing for spaceborne cooperative M-SAR formations with nonzero XT baselines.

calculated as follows [29]:

$$\varphi_c = \frac{1}{2}\left(\hat{\varphi}_{0,n} - \hat{\varphi}_{n,0}\right) + \varphi_{cal} \tag{2}$$

where $\hat{\varphi_{0,n}}$ and $\hat{\varphi_{n,0}}$ are the peak phases of the synchronization signals from the primary satellite and the nth secondary satellite, respectively; φ_{cal} is the internal calibration phase. Further, the high-accuracy compensation phase $\varphi_{syn,n}$ can be obtained through the Kalman filter and interpolation [31]. Finally, compensate $\varphi_{syn,n}$ into the echo signals of the nth secondary satellite.

B. Platform Mismatch Calibration

The receiving links of different secondary satellites are also independent, and the platform mismatch error caused by the hardware link and atmosphere must be considered [32], [33]. A method called azimuth cross correlation can be used in calibration [34] and the excellent effect can be achieved. Assume that the echo signals of every secondary satellite after the synchronization phase error compensation is $s_n(\eta, \tau)$, and $n = 1, 2, 3$ in this article. Take the 1-th secondary satellite as the reference secondary satellite, and the relationship between the echo signals in the range frequency domain is given as follows [34]:

$$S_m(\eta, f_\tau) = S_1\left(\eta - \frac{\Delta b_{\mathrm{AT},m}}{2v_{s,m}}, f_\tau\right) \cdot \exp\left(j2\pi f_\tau \Delta\tau_m\right) \cdot \exp\left(j\varphi_m\right) \tag{3}$$

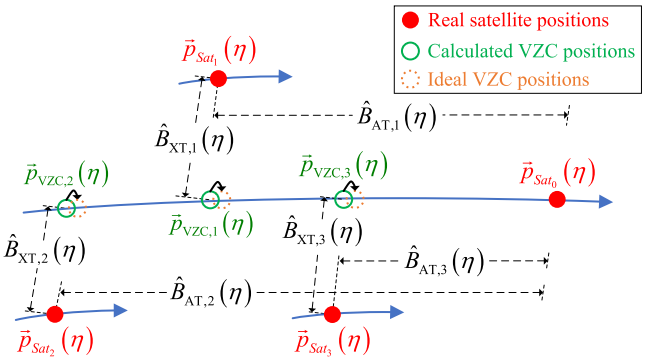

Fig. 6. Diagram of calculating VZC positions of secondary satellites $Sat_n (n = 1, 2, 3)$, which takes the proposed M-SAR formation in this article as an example.

where m refers to subscripts of other secondary satellites other than the reference secondary satellite, and $m = 2, 3$ in this article; η and τ are the range and azimuth time, respectively; f_τ represents the range frequency; $\Delta b_{\mathrm{AT},m}$ is the phase center distance between the mth secondary satellite and the reference secondary satellite; $v_{s,m}$ is the velocity of the mth secondary satellite; φ_m and $\Delta\tau_m$ are the constant phase error and the range sampling time delay, respectively, which is the error that needs to be estimated and compensated.

Perform the operation of azimuth cross correlation to the m echo signals, and the constant phase error φ_m and the range sampling time delay $\Delta\tau_m$ can be obtained as follows [34]:

$$\varphi_m = \arg\left(E_a\left[S_1^*(\eta, f_\tau) \cdot S_m(\eta, f_\tau)\right]\right) - f_\tau \frac{\partial\left(\arg\left(E_a\left[S_1^*(\eta, f_\tau) \cdot S_m(\eta, f_\tau)\right]\right)\right)}{\partial f_\tau} \tag{4}$$

$$\Delta\tau_m = \frac{1}{2\pi}\frac{\partial\left(\arg\left(E_a\left[S_1^*(\eta, f_\tau) \cdot S_m(\eta, f_\tau)\right]\right)\right)}{\partial f_\tau} \tag{5}$$

where $E_a[\cdot]$ denotes averaging operation along the azimuth direction.

C. Nonzero XT Baselines Compensation

Nonzero XT baselines compensation based on MoCo technology is the core step of the proposed method. After the phase error caused by nonzero XT baselines in the echo signal is eliminated, the relevant azimuth reconstruction algorithm can be used to obtain the unambiguous echo signal.

1) Calculate Virtual-Zero-Cross (VZC) Positions: Firstly, calculate the VZC positions of all secondary satellites. The so-called VZC positions refer to the positions of the Sat_n relative to the Sat_0 when there is no XT baseline, as shown in Fig. 6. Suppose coordinates of the Sat_0 and every Sat_n are $\vec{p}_{Sat_0}(\eta)$ and $\vec{p}_{Sat_n}(\eta)$, respectively. Calculate the length of AT baselines from the every Sat_n to the Sat_0, and denote them as $\hat{B}_{\mathrm{AT},n}(\eta)$. It should be noted that the calculation of baselines may be deviated, and we will estimate this deviation and correct it in the subsequent step.

Then, the Range-Doppler (RD) geolocation algorithm [35] is used to obtain ground aiming point (GAP) coordinates and

zero-Doppler (ZD) vectors of the Sat_0. Assuming that GAP coordinates are represented as $\vec{p}_{\eta,k}$, where η indicates the η-th azimuth moment and k represents the kth ZD vector in this period. Thus, the ZD vector at the ηth azimuth moment corresponding to $\vec{p}_{\eta,k}$ can be calculated as $\vec{l}_{\mathrm{ZD},\eta,k}(\eta) = \vec{p}_{Sat_0}(\eta) - \vec{p}_{\eta,k}$. At any azimuth moment, the cross product of any two ZD vectors is performed to obtain the forward vector $\vec{l}_{f,0}(\eta)$ of the Sat_0 at this moment. Thus, the VZC positions of the every Sat_n relative to the Sat_0 can be calculated as

$$\vec{p}_{\mathrm{VZC},n}(\hat{\eta}) = \vec{p}_{Sat_0}(\eta) + \vec{l}_{f,0}(\eta) \cdot \hat{B}_{\mathrm{AT},n}(\eta) \tag{6}$$

where $\hat{\eta}$ indicates that there may be deviation in azimuth direction because the calculated VZC positions may deviate from the ideal case.

2) First-Order Error Compensation: The slant range error specific to the scene center between the every Sat_n and the corresponding VZC position is compensated in the first-order error compensation. Assuming that the coordinate of the scene center is $\vec{p}_0$, and the slant range error can be calculated as

$$\Delta R_{0,n}(\hat{\eta}) = |\vec{p}_{\mathrm{VZC},n}(\hat{\eta}) - \vec{p}_0| - |\vec{p}_{Sat_n}(\eta) - \vec{p}_0|. \tag{7}$$

Thus, first-order phase error compensation for the received echoes is performed as

$$s_n(\tau, \hat{\eta}) = s_n(\tau, \eta) \cdot \exp\left[j4\pi \frac{\Delta R_{0,n}(\hat{\eta})}{\lambda}\right] \tag{8}$$

where $s_n(\tau, \eta)$ is the echo signals after preprocessing. Then, the range resampling is performed as

$$s_n(\tau, \hat{\eta}) = \mathrm{IFFT}_r\left[\mathrm{FFT}_r\left[s_n(\tau, \hat{\eta})\right] \cdot \exp\left(j4\pi \frac{\Delta R_{0,n}(\hat{\eta})}{c} f_\tau\right)\right] \tag{9}$$

where c is speed of light; f_τ represents the range frequency; $\mathrm{FFT}_r[\cdot]$ and $\mathrm{IFFT}_r[\cdot]$ refer to Fast Fourier Transform and Inverse Transform in range direction.

3) Second-Order Error Compensation: The residual slant range error specific to all sampling points in the scene is compensated in the second-order error compensation. Firstly, pulse compression in range direction is performed using the matched filter $\mathrm{H}_r(f_\eta)$ as follows:

$$\mathrm{H}_r(f_\eta) = \exp\left(j\pi \frac{f_\tau^2}{K_r}\right) \tag{10}$$

$$s_n(\tau, \hat{\eta}) = \mathrm{IFFT}_r\left[\mathrm{FFT}_r\left[s_n(\tau, \hat{\eta})\right] \cdot \mathrm{H}_r(f_\eta)\right] \tag{11}$$

where K_r is range frequency-modulated rate. Secondly, divide the range directions into K segments. Use the RD geolocation algorithm to calculate the GAP coordinates and ZD vectors in kth range segment of the Sat_0 in every azimuth moment in combination with Digital Elevation Model, where $k = 1, 2, \ldots, K$. The slant range error between every Sat_n and the corresponding VZC position relative to GAP coordinates $\vec{p}_{\eta,k}$ can be calculated as

$$\Delta R_{k,n}(\hat{\eta}) = |\vec{p}_{\mathrm{VZC},n}(\hat{\eta}) - \vec{p}_{\eta,k}| - |\vec{p}_{Sat_n}(\eta) - \vec{p}_{\eta,k}|. \tag{12}$$

Thus, the residual slant range error can be obtained as

$$\delta R_{k,n}(\hat{\eta}) = \Delta R_{k,n}(\hat{\eta}) - \Delta R_{0,n}(\hat{\eta}). \tag{13}$$

Then, the interpolation along the range direction is carried out to obtain the residual slant range error $\delta R_n(\hat{\eta})$ of all sampling points in the scene, and phase error compensation is performed as follows:

$$s_n(\tau, \hat{\eta}) = s_n(\tau, \hat{\eta}) \cdot \exp\left[j4\pi \frac{\delta R_n(\hat{\eta})}{\lambda}\right] \tag{14}$$

4) Azimuth Resampling: As shown in Fig. 6, there may be deviations between calculated VZC positions and ideal VZC positions in azimuth direction, which is caused by the inaccurate calculation of AT baselines $\hat{B}_{\mathrm{AT},n}(\eta)$. These deviations can be estimated by an optimization problem. The coordinate of Sat_0 (precision), AT baselines (deviation), and XT baselines (deviation) are used to estimate the coordinates of Sat_n, and the distance between the estimated and real coordinates of Sat_n can be calculated. When the distance is small enough, it can be considered that the estimated coordinates of Sat_n are precise enough, i.e., the estimated baselines are precise enough. Thus, we can let $\hat{\boldsymbol{B}}_n(\eta) = \{\hat{B}_{\mathrm{AT},n}(\eta), \hat{B}_{\mathrm{XT},n}(\eta)\}$ be the estimated baselines, and the distance $D[\hat{\boldsymbol{B}}_n(\eta)]$ between the estimated and real coordinates of Sat_n is chosen as the criterion for optimization.

The forward vector $\vec{l}_{f,0}(\eta)$ of the Sat_0 and the forward vectors $\vec{l}_{f,n}(\eta)$ of the Sat_n are used to perform the cross product, and the vectors $\vec{l}_{\perp,n}(\eta)$ along the XT baselines direction can be obtained. Thus, the estimated coordinates of Sat_n can be calculated as follows:

$$\vec{p}_{Sat_n}(\hat{\eta}) = \vec{p}_{\mathrm{VZC},n}(\hat{\eta}) + \vec{l}_{\perp,n}(\eta) \cdot \hat{B}_{\mathrm{XT},n}(\eta) \tag{15}$$

where $\vec{p}_{\mathrm{VZC},n}(\hat{\eta})$ can be obtained according to (6). Thus, the distance between the estimated and real coordinates of Sat_n is given as follows:

$$D\left[\hat{\boldsymbol{B}}_n(\eta)\right] = \|\vec{p}_{Sat_n}(\hat{\eta}) - \vec{p}_{Sat_n}(\eta)\| \tag{16}$$

where $\|\cdot\|$ denotes the module of a vector. Therefore, the optimal estimation of baselines is

$$\hat{\boldsymbol{B}}_n(\eta) = \arg\min_{\hat{\boldsymbol{B}}_n(\eta)} D\left[\hat{\boldsymbol{B}}_n(\eta)\right]. \tag{17}$$

Some optimal methods, such as steepest descent method and Newton method, have been studied to solve the unconstrained optimization problem in (17). The gradient descent method (GDM) is used here as an example. The optimal estimated baselines $\hat{\boldsymbol{B}}_{n,opt}(\eta)$ are obtained when the last iteration is done. Based on GDM, the steps for the optimization problem are given as follows [36]:

Step 1 (*Initialization):* Given initial values of baselines $\hat{\boldsymbol{B}}_{n,0}(\eta)$

Step 2: Calculate the search direction. $\Delta\hat{\boldsymbol{B}}_{n,j}(\eta) = \nabla D[\hat{\boldsymbol{B}}_{n,j}(\eta)]$.

Step 3 (Linear search): Choose step size t via exact or backtracking line search.

Step 4 (Update): Calculate $\hat{\boldsymbol{B}}_{n,j+1}(\eta)$. $\hat{\boldsymbol{B}}_{n,j+1}(\eta) = \hat{\boldsymbol{B}}_{n,j}(\eta) + t \cdot \Delta\hat{\boldsymbol{B}}_{n,j}(\eta)$.

Step 5: If the stopping criterion is satisfied, stop; otherwise, return to ***step2***.

The $\nabla D[\hat{\boldsymbol{B}}_n(\eta)]$ can be expressed as

$$\nabla D\left[\hat{\boldsymbol{B}}_n(\eta)\right] = \left[\frac{\partial D\left[\hat{\boldsymbol{B}}_n(\eta)\right]}{\partial \hat{B}_{\mathrm{AT},n}(\eta)}, \frac{\partial D\left[\hat{\boldsymbol{B}}_n(\eta)\right]}{\partial \hat{B}_{\mathrm{XT},n}(\eta)}\right]. \quad (18)$$

Thus, the deviations between the calculated and ideal VZC positions can be calculated as follows:

$$\Delta\hat{B}_{\mathrm{AT},n}(\eta) = \hat{B}_{\mathrm{AT},n,opt}(\eta) - \hat{B}_{\mathrm{AT},n}(\eta) \quad (19)$$

where $\hat{B}_{\mathrm{AT},n,opt}(\eta)$ is obtained from $\hat{\boldsymbol{B}}_{n,opt}(\eta)$. Thus, the sinc interpolation is used in azimuth resampling to compensate deviations of VZC positions in azimuth direction.

D. Reconstruction Processing

After eliminating the extra phase error introduced by the nonzero XT baseline, the physical meaning of signal acquisition is transformed into the case that acquires echoes along only the AT direction, and the spacing of the receiving phase centers is the length of AT baselines between the Sat_n and the Sat_0. Select the Sat_1 as the reference secondary satellite in this article, which is similar to the reference receive channel in the multichannel SAR system, and Sat_m refers to other secondary satellites other than the reference secondary satellite. Thus, the traditional reconstruction method based on the filter bank [7] is adopted in this article.

The reconstruction filter $\mathbf{P}[f_\eta; \Delta x_n(\eta)]$ is adopted as follows:

$$\mathbf{P}\left[f_\eta; \Delta x_n(\eta)\right] = \mathbf{H}^{-1}\left[f_\eta; \Delta x_n(\eta)\right] \quad (20)$$

where $\Delta x_n(\eta)$ represents the spacing between the Sat_n and the Sat_1. Besides, the elements in the prefilter $\mathbf{H}[f_\eta; \Delta x_n(\eta)]$ can be expressed as follows [7]:

$$H_n\left[f_\eta; \Delta x_n(\eta)\right] = \exp\left[-j\pi \frac{\Delta x_n(\eta)}{v_{s,n}} f_\eta\right] \quad (21)$$

where $v_{s,n}$ is the velocity of the nth secondary satellite; f_η refers to the azimuth frequency.

E. Imaging Processing

After reconstruction processing, the unambiguous echo signal is obtained. Considering the approximation of the quasi-monostatic configuration is still satisfied in the cooperative M-SAR formation; the imaging method proposed by Bamler et al. for BiSAR imaging can be used for [23]. Thus, the imaging geometry of the cooperative M-SAR formation can be considered as the geometry between the Sat_0 and the reference secondary satellite[2] Sat_1.

The equivalent velocity v_e is the most important parameter in the linear track case. For moderate bistatic configurations, the slant range history can be approximated when some assumptions are satisfied [23]

$$R(\eta) \approx \tilde{R}(\eta) = \sqrt{R_0^2 + v_e^2\eta^2} \quad (22)$$

where R_0 is the closest slant range. For the sake of accommodating orbit curvature, a solution of the equivalent velocity is given as follows [37]:

$$v_e = \sqrt{R_0 \cdot \ddot{R}(0)}. \quad (23)$$

This solution is optimal for the center of the aperture but degenerates toward its boundaries. Thus, the best approximation is to use the least mean square error fit over the entire aperture time [23], [37]. In the imaging algorithm proposed in this article, the range-variant and azimuth-variant *equivalent velocity*, i.e., *partitioned equivalent velocity*, is adopted, so as to achieve fine focusing of the entire scene including edge points.

Thus, the slant range history of the reference secondary satellite Sat_1 corresponding to the reference point of the scene can be given by

$$R_{bi}(\eta) = |\vec{p}_{Sat_0}(\eta) - \vec{p}_0| + |\vec{p}_{Sat_1}(\eta) - \vec{p}_0|. \quad (24)$$

Using the approximation of quasi-monostatic, the history given in (24) can be expressed as

$$R_{mono}(\eta) = \frac{R_{bi}(\eta)}{2} \cong \sqrt{R_{0,ref}^2 + v_{e,ref}^2(\eta - \eta_0)^2} \quad (25)$$

where the subscript ref refers to "reference." Using the method of minimum mean square error to fit $[R_{bi}(\eta)/2]^2$, the closest slant range $R_{0,ref}$ and the equivalent velocity $v_{e,ref}$ of the reference point of the scene can be obtained.

The first step of the imaging processing is bulk range processing applied in 2-D frequency domain, which includes range cell migration correction (RCMC), secondary range compression (SRC), and the compensation of all higher-order phase terms for all points located at the reference range [23]. The transfer function is given as follows [23]:

$$\begin{aligned} H_R(f_\eta, f_\tau; R_{0,ref}) &= \exp\left(-j\frac{4\pi}{\lambda} R_{0,ref} \cdot \left[\sqrt{(f_0+f_\tau)^2 - \frac{c^2 f_\eta^2}{4v_{e,ref}^2}}\right.\right. \\ &\quad \left.\left. + \sqrt{1 - \frac{c^2 f_\eta^2}{4v_{e,ref}^2}}\right] - j\pi\frac{f_\tau^2}{K_r}\right) \end{aligned} \quad (26)$$

where f_0 is the carrier frequency.

Afterward, the differential RCMC (DRCMC) is performed in the RD domain to correct the residual range cell migration (RCM) of targets at ranges of $R_{0,i} \neq R_{0,ref}$ by sinc interpolation, as well as the space-variant correction in range direction [23]

$$\begin{aligned} \delta R(f_\eta; R_{0,i}, v_{e,i}) &= \Delta R(f_\eta; R_{0,i}, v_{e,i}) \\ &\quad - \Delta R(f_\eta; R_{0,ref}, v_{e,ref}) \end{aligned} \quad (27)$$

where $\Delta R(f_\eta; R_{0,i}, v_{e,i})$ is the RCM at the ith range gate, which $i = 1, 2, \ldots, N_r$, and N_r is the sampling numbers in range;

[2]It is necessary to ensure that the reference secondary satellite during the imaging processing is consistent with the reference secondary satellite during the reconstruction processing.

$\Delta R(f_\eta; R_{0,ref}, v_{e,ref})$ is the RCM at the reference range gate; and the specific form is expressed as follows:

$$\Delta R\left(f_\eta; R_{0,i}, v_{e,i}\right) = \frac{R_{0,i}}{D\left(f_\eta; v_{e,i}\right)} - R_{0,i} \tag{28}$$

where $D(f_\eta; v_e)$ is the migration factor in the RD domain, and it is given by

$$D\left(f_\eta; v_{e,i}\right) = \sqrt{1 - \frac{\lambda^2 f_\eta^2}{4v_{e,i}^2}} \tag{29}$$

where $v_{e,i}$ represents the equivalent velocity corresponding to the ith range gate.

In the case of wide swath, the residual high-order phase errors caused by bulk range processing cannot be ignored. Further, the residual space-variant characteristics in range direction are considered in order to achieve the high phase-preserve imaging. Therefore, the signal of the RD domain after DRCMC is divided into N blocks along the range direction and transformed into 2-D frequency domain. Then, a range-variant transfer function is given by

$$H_{src,var}\left(f_\eta, f_\tau; R_{0,n}, v_{e,n}\right) = \exp\left(-j\frac{4\pi\left(R_{0,n} - R_{0,ref}\right)}{c} \cdot \left[\frac{1 - D\left(f_\eta; v_{e,n}\right)^2}{2!f_0 D\left(f_\eta; v_{e,n}\right)^3} f_\tau^2 - \frac{1 - D\left(f_\eta; v_{e,n}\right)^2}{3!f_0^2 D\left(f_\eta; v_{e,n}\right)^5} f_\tau^3 + \Phi_{high}\right]\right) \tag{30}$$

where Φ_{high} refers to high-order residual phase; $n = 1, 2, \ldots, N$; $R_{0,n}$ and $v_{e,n}$ are the closest slant range and the equivalent velocity corresponding to each block of the signal. Use (30) to complete the compensation of each block of the signal in the 2-D frequency domain. Then, transform each block of the signal into the RD domain for splicing. It should be noted that the purpose of segmenting the signal in range direction is to compensate the residual phase error after the bulk range processing, and will not cause the difference in imaging quality of each block. After the above operation, the space-variant characteristic in range direction can be corrected through the range-variant *equivalent velocity*.

Finally, the imaging processing is azimuth compression, which the space-variant characteristic correction in azimuth direction is also performed in this step. The signal in the RD domain is divided into M blocks along the azimuth direction, and the azimuth matched filter of each block is constructed according to the equivalent velocity $v_{e,m}$ and closest slant range $R_{0,m}$ of the reference range gate corresponding to the each block

$$H_{AC,var}\left(f_\eta; R_{0,m}, v_{e,m}\right) = \exp\left[-j\frac{4\pi R_{0,m}\left(1 - D\left(f_\eta; v_{e,m}\right)\right)}{\lambda}\right] \tag{31}$$

where $m = 1, 2, \ldots, M$. Use the azimuth matched filters of (31) to perform M times matched filtering on the overall signal in azimuth, i.e., multiple the signal and the matched filter in the RD domain and then transform them into the azimuth time domain to obtain all imaging results after matched filtering. In the azimuth time domain, the images focused by each filters are extracted and spliced according to the segmentation strategy to obtain a complete focusing image. So far, the 2-D space-variant characteristics are compensated, and all pixels in the scene (including edge points) can achieve high phase-preserve fine focusing.

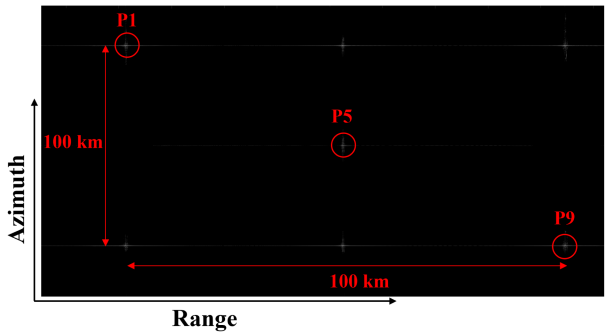

Fig. 7. Nine simulated point targets which are processed by the proposed method in this article.

TABLE II
SIMULATION PARAMETERS

Parameters	Value
Satellite height	984 km
Satellite velocity	7.45 km/s
Carrier frequency	9.6 GHz
Pulsewidth	50 μs
Bandwidth	300 MHz
Sampling rate	360 MHz
Pulse repetition frequency	3200 Hz
Numbers of received satellites	3
$B_{\mathrm{XT},1}$	300.25∼300.36 m
$B_{\mathrm{XT},2}$	-300.30∼-300.21 m
$B_{\mathrm{XT},3}$	300.22∼300.32 m

IV. SIMULATION

In order to demonstrate the validity of the proposed method, the simulations of point targets and distributed targets are carried out in this section. An array composed of nine point targets is adopted in the simulation, which are laid on a 100 km×100 km grid in ground range/azimuth directions, and the geometry of the designed scene is presented in Fig. 7. P5 is the center of the scene (which is also the reference point target). In order to evaluate the focusing effect of the imaging algorithm on the edge of aperture, point targets of P1, P5, and P9 are chosen for analyzing the imaging quality without loss of generality. Simulation parameters are listed in Table II, and the X-band SAR system is used to reflect the goal of HRWS. In addition, parameters of the satellite orbit are from the spaceborne M-SAR formation proposed in this article. A rectangular window is used in both the range and azimuth direction instead of a real antenna pattern, i.e., no weight is used, in order to facilitate the quantitative evaluation of imaging results.

The influence of nonzero XT baselines on the azimuth reconstruction algorithm can be observed from the azimuth spectrum of one point target, as shown in Fig. 8. It can be seen from

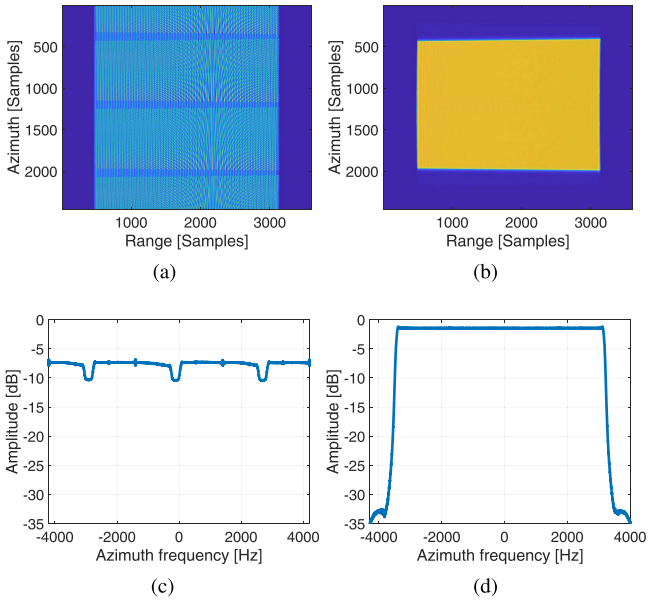

Fig. 8. Azimuth spectrum of one point target after performing the azimuth reconstruction algorithm. (a) and (c) The error introduced by nonzero XT baselines is not compensated. (b) and (d) The error introduced by nonzero XT baselines is compensated by the proposed method. The first line is in the 2-D frequency domain (the range and azimuth axis are scaled several times for the convenience of presentation), and the second line is in the 1-D frequency domain.

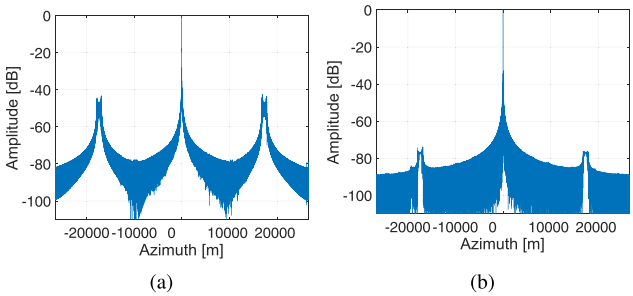

Fig. 9. A complete imaging result of the azimuth profile of the reference point (P5), and the nonbandlimited real antenna patterns in azimuth direction is considered. (a) The result of simulated single satellite case. (b) The result processed by the proposed scheme after merging simulated three satellites' echoes.

Fig. 8(a) and (c) that when the error introduced by nonzero XT baselines is not compensated, the reconstruction method fails completely. The spectrum is split into some segments in azimuth direction, which is obviously wrong. After performing compensation with the proposed method, the spectrum within the effective frequency band is well reconstructed as shown in Fig. 8(b) and (d).

The imaging results processed by the proposed method are presented in Fig. 11, and contour plots, azimuth profiles, and range profiles are given. It can be seen that the reference point (P5) and the edge points (P1 and P9) are all well focused, and the problem of space-variant characteristics, i.e., the defocusing of edge points, is solved well. The evaluation of imaging quality is given in Table III. The peak sidelobe ratio (PSLR), the integral sidelobe ratio (ISLR), and the pulse response width (IRW) in

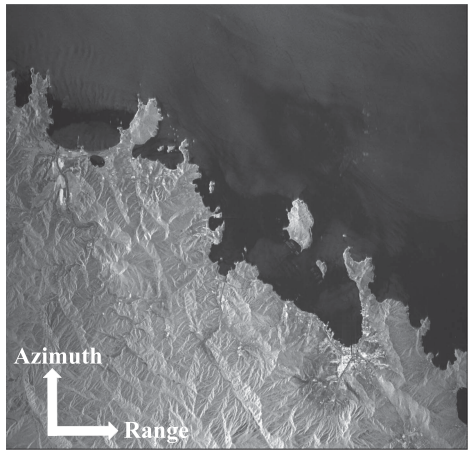

Fig. 10. Imaging result of distributed targets processed by the proposed method. The selected position is the coast along the northeast of China (42.16°N 130.22°E).

both directions are almost the same as those in theoretical values [38], and theoretical values are also given in Table III. Thus, according to the simulation results of point targets, the proposed imaging method shows the excellent focusing performance for the scenario where spaceborne M-SAR system is used to achieve high-resolution (below 1 m) and wide swath width (100 km).

In addition, it is necessary to verify whether the proposed method can achieve high phase-preserving. Commonly, the phase of the slant range R of the point target that needs to be retained after the imaging processing should be $\exp(j4\pi R/\lambda)$. The phase-preserving evaluation is to obtain the phase difference between the phase of the focused point target and the abovementioned phase that needs to be retained, and the evaluation results are also shown in Table III. Similarly, taking the P1, P5, and P9 as examples. Under the focusing of the proposed method, the phase-preserving accuracy of the whole scene is approximately 0.1°, which is small enough.

The suppression effect of the proposed method on the azimuth ambiguity is shown in Fig. 9, and the nonbandlimited real antenna patterns in azimuth direction is considered here. Obvious ghosts appear in the simulated single satellite case due to the undersampling in azimuth direction, as shown in Fig. 9(a). The result processed by the proposed method after merging simulated three satellites' echoes is shown in Fig. 9(b). The performance of the azimuth ambiguity is greatly improved, and the intensity of ghosts is weakened by about -30 dB. In fact, the azimuth ambiguity is worse when the traditional filter bank method is used to deal with the case of large AT baselines. This problem is not the focus of this article, and the methods proposed in [8], [25] can be used to solve the reconstruction problem of large AT baselines.

Finally, the simulation of distributed targets is carried out to verify the performance of the proposed method, and a real SAR image that is extracted by GaoFen-3 is used as the target radar cross-sectional information for simulation purpose. The selected position is the coast along the northeast of China (42.16°N 130.22°E), and the imaging result of distributed targets

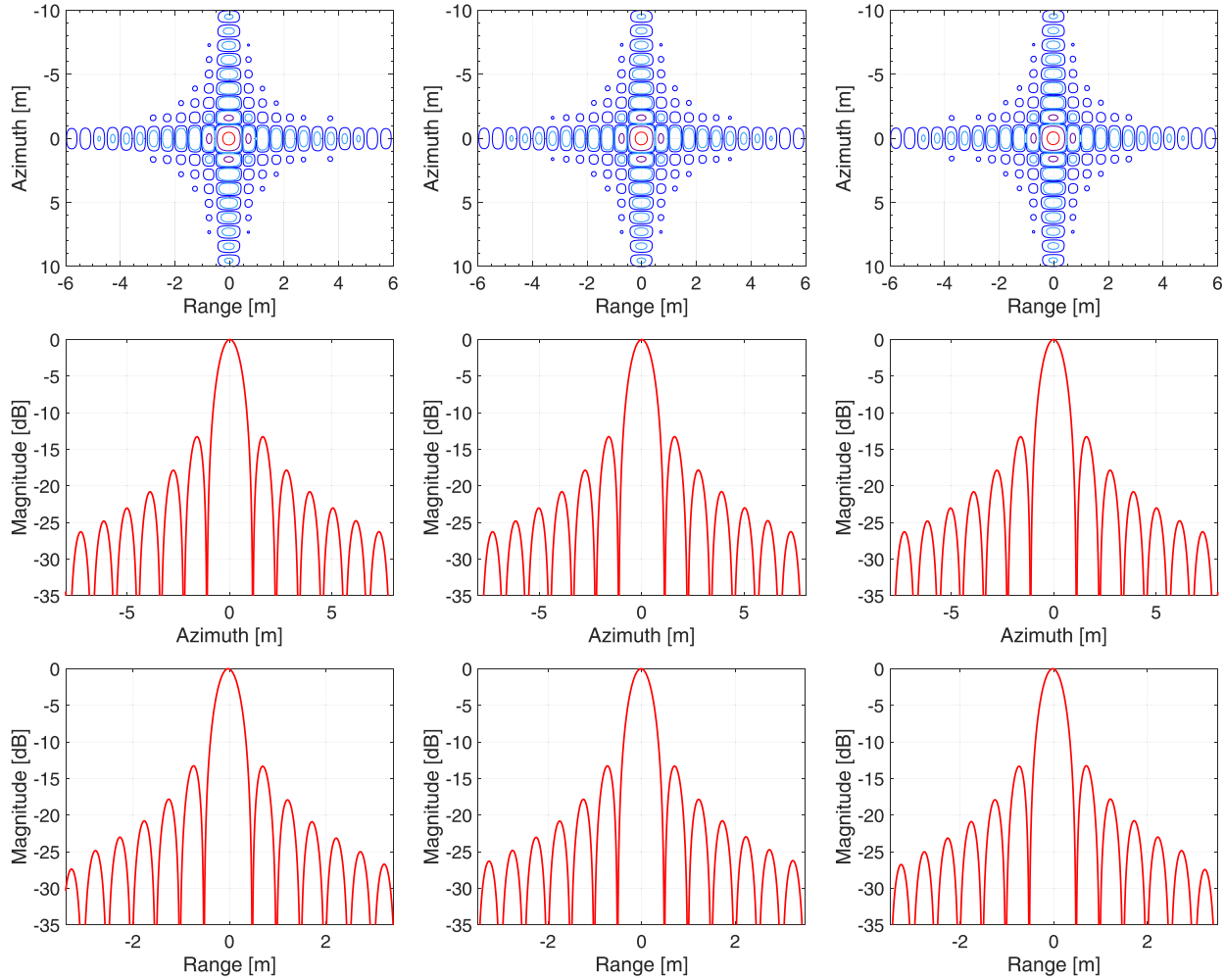

Fig. 11. Imaging results of point targets processed by the proposed method. Contour plots (the first line), azimuth profiles (the second line) and range profiles (the third line) of P1 (the first column), P5 (the second column) and P9 (the third column).

TABLE III
EVALUATION OF IMAGING QUALITY IN POINT TARGETS SIMULATION

Targets	Azimuth			Range			Residual Phase Error
	IRW(m)	PSLR(dB)	ISLR(dB)	IRW(m)	PSLR(dB)	ISLR(dB)	
Theoretical	0.992	-13.26	-9.80	0.443	-13.26	-9.80	0°
P1	0.995	-13.28	-9.95	0.444	-13.27	-9.91	0.0545°
P5	0.994	-13.27	-9.94	0.444	-13.27	-9.88	0.0423°
P9	0.995	-13.28	-9.95	0.445	-13.26	-9.90	0.0625°

processed by the proposed method is shown in Fig. 10. The fine imaging of the M-SAR formation with nonzero XT baselines can be achieved by the proposed method, and the good suppression of the ambiguities is also achieved.

V. CONCLUSION

In the M-SAR formation, AT baselines are necessary to achieve the HRWS, and the XT separation may be existed due to orbital safety and application potentials. Thus, how to deal with the problem of nonzero XT baselines for the signal processing of M-SAR needs to be considered urgently. On the other hand, different motion vectors of multiple satellites caused by the Helix formation will lead to the difference of the closest slant range and Doppler characteristics at the same range gate. Thus, space-variant characteristics pose challenge to the focusing and phase-preserving of the Bi/M-SAR imaging, which needs to be solved in the imaging algorithm. Firstly, an M-SAR formation which consists of one transmitting primary satellite and three receiving only secondary satellites are demonstrated in this article. Afterward, an imaging method for spaceborne cooperative M-SAR formations with nonzero XT baselines is proposed, which is aimed to solve the extra error introduced by nonzero XT baselines and the problem of space-variant characteristics.

Finally, the simulations of point targets and distributed targets are carried out to verify the proposed method, and the results demonstrate the effectiveness of the proposed method.

REFERENCES

[1] M. D'Errico, *Distributed Space Missions for Earth System Monitoring*. New York, NY, USA: Springer, 2013.

[2] R. Wang and Y. Deng, *Bistatic SAR System and Signal Processing Technology*. Singapore: Springer, 2018.

[3] A. Moreira, P. Prats-Iraola, M. Younis, G. Krieger, I. Hajnsek, and K. P. Papathanassiou, "A tutorial on synthetic aperture radar," *IEEE Geosci. Remote Sens. Mag.*, vol. 1, no. 1, pp. 6–43, Mar. 2013.

[4] G. Krieger and A. Moreira, "Spaceborne bi- and multistatic SAR: Potential and challenges," *IEE Proc.-Radar, Sonar Navigation*, vol. 153, no. 3, pp. 184–198, Jun. 2006.

[5] A. Moreira et al., "Multi-baseline spaceborne SAR imaging," in *Proc. IEEE Int. Geosci. Remote Sens. Symp.*, 2016, pp. 1420–1423.

[6] J. Mittermayer et al., "MirrorSAR: An HRWS add-on for single-pass multi-baseline SAR interferometry," *IEEE Trans. Geosci. Remote Sens.*, vol. 60, pp. 1–18, Dec. 2021.

[7] G. Krieger, N. Gebert, and A. Moreira, "Unambiguous SAR signal reconstruction from nonuniform displaced phase center sampling," *IEEE Geosci. Remote Sens. Lett.*, vol. 1, no. 4, pp. 260–264, Oct. 2004.

[8] N. Sakar, M. Rodriguez-Cassola, P. Prats-Iraola, and A. Moreira, "Azimuth reconstruction algorithm for multistatic SAR formations with large along-track baselines," *IEEE Trans. Geosci. Remote Sens.*, vol. 58, no. 3, pp. 1931–1940, Mar. 2020.

[9] N. Sakar, M. Rodriguez-Cassola, P. Prats-Iraola, A. Reigber, and A. Moreira, "Analysis of geometrical approximations in signal reconstruction methods for multistatic sar constellations with large along-track baseline," *IEEE Geosci. Remote Sens. Lett.*, vol. 15, no. 6, pp. 892–896, Jun. 2018.

[10] P. Guccione, A. Monti Guarnieri, F. Rocca, D. Giudici, and N. Gebert, "Along-track multistatic synthetic aperture radar formations of minisatellites," *Remote Sens.*, vol. 12, no. 1, Jan. 2020, Art. no. 124.

[11] O. Dogan, F. Uysal, and P. L. Dekker, "Unambiguous recovery of multistatic SAR data for nonzero cross track baseline case," *IEEE Geosci. Remote Sens. Lett.*, vol. 19, pp. 1–5, 2022.

[12] C. Zhang, Z. Ding, and Z. Dong, "A two-step channel mismatch estimation and compensation method for distributed MC SAR," *Int. J. Remote Sens.*, vol. 42, no. 18, pp. 7031–7052, Jun. 2021.

[13] T. Kraus, G. Krieger, M. Bachmann, and A. Moreira, "Spaceborne demonstration of distributed SAR imaging with TerraSAR-X and TanDEM-X," *IEEE Geosci. Remote Sens. Lett.*, vol. 16, no. 11, pp. 1731–1735, Nov. 2019.

[14] T. Kraus, M. Bachmann, and G. Krieger, "Topography correction for distributed SAR imaging: A case study for TerraSAR-X and TanDEM-X," in *Proc. 12th Eur. Conf. Synth. Aperture Radar*, 2018, pp. 1–5.

[15] O. Loffeld, H. Nies, V. Peters, and S. Knedlik, "Models and useful relations for bistatic SAR processing," *IEEE Trans. Geosci. Remote Sens.*, vol. 42, no. 10, pp. 2031–2038, Oct. 2004.

[16] K. Natroshvili, O. Loffeld, H. Nies, A. Ortiz, and S. Knedlik, "Focusing of general bistatic SAR configuration data with 2-D inverse scaled FFT," *IEEE Trans. Geosci. Remote Sens.*, vol. 44, no. 10, pp. 2718–2727, Oct. 2006.

[17] R. Wang et al., "Processing the azimuth-variant bistatic SAR data by using monostatic imaging algorithms based on two-dimensional principle of stationary phase," *IEEE Trans. Geosci. Remote Sens.*, vol. 49, no. 10, pp. 3504–3520, Oct. 2011.

[18] R. Wang, O. Loffeld, Q. Ul-Ann, H. Nies, A. Medrano Ortiz, and A. Samarah, "A bistatic point target reference spectrum for general bistatic SAR processing," *IEEE Geosci. Remote Sens. Lett.*, vol. 5, no. 3, pp. 517–521, Jul. 2008.

[19] Y. L. Neo, F. Wong, and I. G. Cumming, "A two-dimensional spectrum for bistatic SAR processing using series reversion," *IEEE Geosci. Remote Sens. Lett.*, vol. 4, no. 1, pp. 93–96, Jan. 2007.

[20] F. H. Wong, I. G. Cumming, and Y. L. Neo, "Focusing bistatic SAR data using the nonlinear chirp scaling algorithmn," *IEEE Trans. Geosci. Remote Sens.*, vol. 46, no. 9, pp. 2493–2505, Sep. 2008.

[21] A. Moreira, J. Mittermayer, and R. Scheiber, "Extended chirp scaling algorithm for air- and spaceborne SAR data processing in stripmap and ScanSAR imaging modes," *IEEE Trans. Geosci. Remote Sens.*, vol. 34, no. 5, pp. 1123–1136, Sep. 1996.

[22] D. Meng, D. Hu, and C. Ding, "Precise focusing of airborne SAR data with wide apertures large trajectory deviations: A chirp modulated back-projection approach," *IEEE Trans. Geosci. Remote Sens.*, vol. 53, no. 5, pp. 2510–2519, May 2015.

[23] R. Bamler, F. Meyer, and W. Liebhart, "Processing of bistatic SAR data from quasi-stationary configurations," *IEEE Trans. Geosci. Remote Sens.*, vol. 45, no. 11, pp. 3350–3358, Nov. 2007.

[24] G. Krieger et al., "TanDEM-X: A satellite formation for high-resolution SAR interferometry," *IEEE Trans. Geosci. Remote Sens.*, vol. 45, no. 11, pp. 3317–3341, Nov. 2007.

[25] N. Sakar, M. Rodriguez-Cassola, P. Prats-Iraola, and A. Moreira, "Sampling analysis and processing approach for distributed SAR constellations with along-track baselines," *IEEE Trans. Geosci. Remote Sens.*, vol. 60, pp. 1–12, 2022.

[26] P. Rosen et al., "Synthetic aperture radar interferometry," *Proc. IEEE*, vol. 88, no. 3, pp. 333–382, Mar. 2000.

[27] M. Younis, R. Metzig, and G. Krieger, "Performance prediction of a phase synchronization link for bistatic SAR," *IEEE Geosci. Remote Sens. Lett.*, vol. 3, no. 3, pp. 429–433, Jul. 2006.

[28] G. Krieger and M. Younis, "Impact of oscillator noise in bistatic and multistatic SAR," *IEEE Geosci. Remote Sens. Lett.*, vol. 3, no. 3, pp. 424–428, Jul. 2006.

[29] D. Liang et al., "The processing framework and experimental verification for the noninterrupted synchronization scheme of LuTan-1," *IEEE Trans. Geosci. Remote Sens.*, vol. 59, no. 7, pp. 5740–5750, Jul. 2021.

[30] G. Krieger and F. De Zan, "Relativistic effects in bistatic synthetic aperture radar," *IEEE Trans. Geosci. Remote Sens.*, vol. 52, no. 2, pp. 1480–1488, Feb. 2014.

[31] D. Liang et al., "A high-accuracy synchronization phase-compensation method based on kalman filter for bistatic synthetic aperture radar," *IEEE Geosci. Remote Sens. Lett.*, vol. 17, no. 10, pp. 1722–1726, Oct. 2020.

[32] F. Queiroz de Almeida, M. Younis, G. Krieger, and A. Moreira, "An analytical error model for spaceborne SAR multichannel azimuth reconstruction," *IEEE Geosci. Remote Sens. Lett.*, vol. 15, no. 6, pp. 853–857, Jun. 2018.

[33] F. Xiao, Z. Ding, Z. Li, and T. Long, "Channel error effect analysis for reconstruction algorithm in dual-channel SAR imaging," *IEEE Geosci. Remote Sens. Lett.*, vol. 17, no. 9, pp. 1563–1567, Sep. 2020.

[34] J. Feng, C. Gao, Y. Zhang, and R. Wang, "Phase mismatch calibration of the multichannel SAR based on azimuth cross correlation," *IEEE Geosci. Remote Sens. Lett.*, vol. 10, no. 4, pp. 903–907, Jul. 2013.

[35] J. C. Curlander, "Location of spaceborne SAR imagery," *IEEE Trans. Geosci. Remote Sens.*, vol. GE-20, no. 3, pp. 359–364, Jul. 1982.

[36] S. Boyd and L. Vandenberghe, *Convex Optimization*. Cambridge, U.K.: Cambridge Univ. Press, 2004.

[37] F. Wong, N. L. Tan, and T. S. Yeo, "Effective velocity estimation for space-borne SAR," in *Proc. IEEE Int. Geosci. Remote Sens. Symp.*, vol. 1, 2000, pp. 90–92.

[38] I. G. Cumming and F. H. Wong, *Digital Processing of Synthetic Aperture Radar Data: Algorithms and Implementation*. Norwood, MA, USA: Artech House, 2005.

Haoyu Lin was born in Fujian, China, in 1995. He received the B.S. degree in electronic information engineering from Hunan University, Changsha, China, in 2018. He is currently working toward the Ph.D. degree with the Department of Space Microwave Remote Sensing System, Aerospace Information Research Institute, Chinese Academy of Science, Beijing, China.

He is currently with the University of Chinese Academy of Sciences, Beijing, China. His research interests include bistatic synthetic aperture radar imaging and signal processing.

Yunkai Deng (Member, IEEE) received the M.S. degree in electrical engineering from the Beijing Institute of Technology, Beijing, China, in 1993.

In 1993, he joined the Institute of Electronics, Chinese Academy of Sciences (IECAS), Beijing, China, where he was involved in antenna design, microwave circuit design, and spaceborne/airborne synthetic-aperture radar (SAR) technology. Since 1993, he has been a Research Fellow with the Department of Space Microwave Remote Sensing System, IECAS. He has been the Leader of several spaceborne/airborne SAR programs and developed some key technologies of spaceborne/airborne SAR. Since 2012, he has been a Principal Investigator with the Helmholtz-Chinese Academy of Sciences (CAS) Joint Research Group, Beijing, China, concerning Spaceborne Microwave Remote Sensing for Prevention and Forensic Analysis of Natural Hazards and Extreme Events. He is a Research Scientist with the University of Chinese Academy of Sciences, Beijing, China. Since 2002, he has authored or coauthored more than 100 articles, of which more than 100 peer-reviewed and well-known journal articles. His research interests include spaceborne/airborne SAR technology for advanced modes, multifunctional radar imaging, and microwave circuit design.

Mr. Deng is a Member of the Scientific Board. He was a recipient of several prizes, including the First and Second Class Rewards of National Defense Science and Technology Progress in 2007, the First Class Reward of the National Scientific and Technological Progress in 2008, the achievements of the Outstanding Award of the CAS in 2009, and the First Class Reward of Army Science and Technology Innovation in 2016, for his outstanding contribution in SAR field.

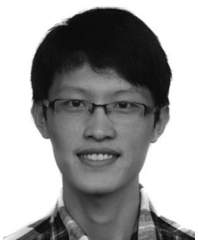

Heng Zhang (Member, IEEE) received the B.S. degree in electronic information science from Nanjing University, Nanjing, China, in 2013, and the Ph.D. degree in communication and information systems from the University of Chinese Academy of Sciences, Beijing, China, in 2018.

In 2018, he joined the Aerospace Information Research Institute, Chinese Academy of Sciences, Beijing, China. His research interests include bistatic synthetic aperture radar imaging and interferometry.

Da Liang (Member, IEEE) received the B.S. degree in microelectronics from Nankai University, Tianjin, China, in 2016, and the Ph.D. degree in communication and information systems from the University of Chinese Academy of Sciences, Beijing, China, in 2021.

In 2021, he joined the College of Marine Technology, Ocean University of China, Qingdao, China. His research interests include synthetic aperture radar (SAR) imaging, SAR internal calibration, synchronization of bistatic SAR systems, and signal processing.

Xiaoxue Jia received the Ph.D. degree in communication and information system from the Institute of Electronics, Chinese Academy of Sciences, Beijing, China, in 2010.

She is currently an Associate Research Fellow with the Department of Space Microwave Remote Sensing System, Aerospace Information Research Institute, Chinese Academy of Sciences. Her research interests include SAR signal processing techniques.